

OPEN ACCESS

Sustainable SiC Composite Anodes, Graphite Accelerated Lithium Storage

To cite this article: Mengjie Yu *et al* 2023 *J. Electrochem. Soc.* **170** 070504

View the [article online](#) for updates and enhancements.

You may also like

- [First-Principles Study of Li-Ion Diffusion Mechanism in Highly Concentrated Li-Salt Electrolyte](#)
Keitaro Sodeyama, Yuki Yamada, Atsuo Yamada *et al.*
- [Low Cost and Metal Free Counter Electrode for Dye Sensitized Solar Cell](#)
Mojgan Kouhanavard, Babak V-Ghaffari and Mikio Miyake
- [Comparing the Lithiation and Sodiation of a Hard Carbon Anode Using In Situ Impedance Spectroscopy](#)
Fabian Linsenmann, Daniel Pritzl and Hubert A. Gasteiger



245th ECS Meeting • May 26-30, 2024 • San Francisco, CA

[Learn more & submit!](#)

Present your work at the leading electrochemistry & solid-state science conference.

Network with academic, government, and industry influencers!

Submit abstracts by December 1, 2023





Sustainable SiC Composite Anodes, Graphite Accelerated Lithium Storage

Mengjie Yu,^{1,*} Eleni Temeche,^{2,**} Sylvio Indris,³ and Richard M. Laine^{1,2,z} 

¹Macromolecular Science and Engineering, University of Michigan, Ann Arbor, Michigan 48109, United States of America

²Department of Materials Science and Engineering, University of Michigan, Ann Arbor, Michigan 48109, United States of America

³Institute for Applied Materials-Energy Storage Systems (IAM-ESS), Karlsruhe Institute of Technology (KIT) Eggenstein-Leopoldshafen 76344, Germany

Realizing more holistic electrification in society to disengage current dependence on nonrenewable fuels requires balancing between energy storage mechanisms and actual environmental benefits gained from the transition from traditional resources. Given that the majority of greenhouse gas emissions in battery value chains originate from material mining and production, silicon carbide (SiC) derived from the agricultural waste, rice hull ash (RHA), is introduced as an environmentally-benign alternate anode material. SiC with hard carbon (SiC/HC) exhibits capacity increases on long-term cycling, reaching capacities of $>950 \text{ mAh g}^{-1}$ competitive with elemental Si with complementary porosity. Herein, a relatively low amount ($<30 \text{ wt\%}$) of graphite added to SiC/HC composites greatly promotes capacity increases while retaining sustainability. Comparison between graphite contents were optimal at $\approx 30 \text{ wt\%}$ graphite (SiC/HC/30G) boosted performance, doubling capacity increase rates and subsequently saving $>70\%$ time to reach target specific capacities at C/10. At 2C, SiC/HC/30G offers enhanced specific capacities at $\approx 220 \text{ mAh g}^{-1}$. The positive effects from the coincidentally formed HC are demonstrated by oxidizing HC to form SiC/O, followed by graphite addition. Experimental post-mortem analyses support that SiC/graphite composites provide a promising solution for implementing agricultural waste-derived material for next-generation lithium storage.

© 2023 The Author(s). Published on behalf of The Electrochemical Society by IOP Publishing Limited. This is an open access article distributed under the terms of the Creative Commons Attribution 4.0 License (CC BY, <http://creativecommons.org/licenses/by/4.0/>), which permits unrestricted reuse of the work in any medium, provided the original work is properly cited. [DOI: 10.1149/1945-7111/ace132]



Manuscript submitted May 1, 2023; revised manuscript received June 19, 2023. Published July 5, 2023. *This paper is part of the JES Focus Issue on Carbon Negative Technologies.*

Supplementary material for this article is available [online](#)

From the pre-industrial era to the 2020s, global warming from human-produced greenhouse gas emissions has increased by $\approx 90\%$.¹ Transportation activities have surpassed electric power generation and account for the largest share ($\approx 27\%$) of U.S. greenhouse gas emissions out of all economic end-use sectors since 2017.²

Greenhouse gas emissions from transportation primarily come from burning fossil fuel for passenger cars, trucks, aircraft, etc. Therefore, replacing petroleum-based vehicles with clean, renewable energy-based vehicles (EVs) is a crucial and urgent problem. The recent increase in EVs on the road represents a start. However, more complete penetration of EVs in the market requires reliable batteries with high energy densities, durability, and much diminished carbon footprints.³ EV batteries are widely expected to deliver energy densities of 350 Wh kg^{-1} and 750 Wh l^{-1} at cell levels to achieve driving ranges $>500 \text{ km}$ and cycling performances >1300 cycles.^{4,5} Pioneering work on innovative electrodes targets increasing energy densities (driving range), extending cycle life,⁶ while reducing production economics and resource expenditures.⁷

Potential improvements in anodes also offer multiple opportunities. The current commercial graphite anode was adopted decades ago due to its high reversibility and conductivity, as well as low cost and well-established processing technologies.^{8–10} However, its theoretical maximum capacity of 375 mAh g^{-1} requires one lithium atom incorporated with six carbon atoms with a $\Delta V \approx 13\%$, which hampers progress toward higher performance rechargeable batteries.^{11,12}

In contrast, Si, with a ten times higher theoretical capacity of 3579 mAh g^{-1} and low working voltage (0.2 V vs Li/Li^+) is believed to be one of the most promising alloy-type anodes.^{13,14} However, direct use of Si has yet to be realized due to low

conductivities and the destructively large volume changes ($\Delta V > 300\%$) during alloying/dealloying with Li.^{15,16}

Unfavorable consequences include electrode deformation, electrical isolation induced by Si particle pulverization and disconnection from the current collector,^{17,18} excessive Li^+ consumption, and increased internal resistance resulting from accumulated solid–electrolyte interfaceinterphase (SEI) layers on fractured particles. Taken together these continuous processes lead to severe capacity deterioration and even safety concerns due to bulging cell packaging.^{19,20}

Among all strategies for alleviating the foregoing challenges, incorporation of silicon in carbonaceous materials such as coating silicon with a carbon surface,^{21–23} constructing porous silicon/carbon structures,^{24–26} or embedding silicon into a carbon matrix are subjects of extensive research as the method offers significant potential advantages.^{27–29} Introducing carbonaceous components may buffer electrode disintegration and enhance the conductivities between silicon particles.^{5,16} However, current silicon/graphite composite anodes typically use low Si contents $< 30 \text{ wt\%}$ to limit total ΔV and retain contacts and conductivities between components,^{30–32} restraining practical energy density improvements accessible using Si anodes.

We previously reported processing SiC with $\approx 15 \text{ wt\%}$ hard carbon (SiC/HC) from rice hull ash (RHA). The accompanying hard carbon can be removed by oxidatively generating (SiC/O) nanocomposites.^{33,34} The SiC/HC anodes exhibit charge/discharge capacities $3\times$ that of current graphite anodes at $>950 \text{ mAh g}^{-1}$ following slow cycling (C/10–C/2), which promotes distinctive capacity increases. The coincidentally formed hard carbon provides positive effects on anode performance. In particular, SiC lithiation/delithiation occurs *without significant ΔV* according to XRD and SEM, suggesting that SiC can compete with porous elemental Si. As discussed above, free volumes equivalent to $3\times$ are required to accommodate the accordion-like behavior of Si anodes.

Furthermore, it is worth noting that metallurgical grade Si metal ($\text{Si}_{\text{MT}} \approx 98\%$ purities) is synthesized via the carbothermal reduction at $\approx 1900 \text{ }^\circ\text{C}$; however, the purities needed for Si anodes are believed

*Electrochemical Society Student Member.

**Electrochemical Society Member.

^zE-mail: talsdad@umich.edu

to be much higher mandating additional, expensive (CO₂ and equipment-intensive) processing steps. While battery-grade graphite (purities >99.9%)³⁵ used today is produced in an environmentally harmful and expensive multistep method that involves heating to ≈3000 °C,^{7,36} in comparison, nanocomposite silica-depleted RHA (SDRHA) can be heated to 1450 °C/Ar to produce SiC/HC. In this aspect, biowaste-derived SiC/HC offers a more environmentally-friendly alternate anode. Furthermore, taking into account the gigawatts of electricity generated by RHA combustion and other value-added materials generated simultaneously from the processes (e.g. precursors for polymer Li⁺ electrolytes,³⁷ Li⁺ supercapacitors electrodes,³⁸ etc), this method has considerable potential as a carbon-neutral and even carbon-negative technology.

The current work is inspired by the developed concept of adding graphite to reduce unnecessary electrolyte decomposition, facilitate anode integrity retention, provide pathways for electron transfer, and consequently improve the performance of silicon-based anodes.^{30,39,40} We find adding graphite to SiC/HC nanocomposites led to a two-fold improvement in rates of capacity increase on cycling, reaching >950 mAh g⁻¹ after 250 cycles. In contrast to the >50 wt% graphite in common Si-based anodes to build sufficient buffer space for silicon and to integrate the multiple species,³⁰ mixing only 30 wt% graphite with the SiC/HC here results in specific capacities competitive with porous Si. Thus, adding a low amount of graphite to boost SiC/HC performance still retains the superiority of greener production processes. Experimental post-mortem studies also investigated the proposed interactions within the SiC/HC + graphite composites.

Experimental

Synthesis of SiC/HC and SiC/O composites with graphite.—The synthesis of SiC using RHA as a starting material was reported in detail recently.³³ In brief, 30–50 wt% of SiO₂ was extracted from RHA (Wadham Energy Inc.) to recover SDRHA with target C:SiO₂ ratios.^{37,38,41} The SDRHA was then carbothermally reduced to generate SiC with hard carbon (SiC/HC ≈ 85/15), while the excess hard carbon can be removed by oxidizing at 500 °C/1 h/O₂ (SiC/O). Commercial graphite supplied from Superior Graphite, was used without further purification to mix with the as-prepared SiC/HC or SiC/O in NMP solvent by low-energy ball milling with yttria-stabilized zirconia media (~3 mm) overnight. The composite weight ratios of graphite to SiC/HC or SiC/O as 7:3 are denoted as SiC/HC/30G and SiC/O/30G, respectively, while those with weight ratios of 9:1 as SiC/HC/10G and SiC/O/10G.

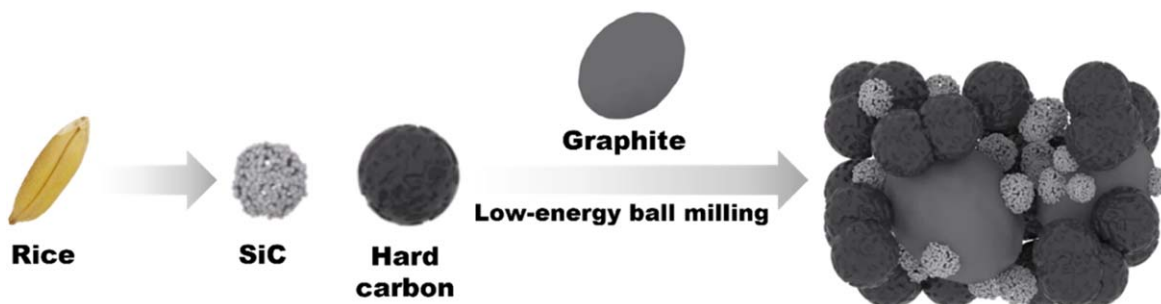
Material characterization.—Basic characterization was conducted after removing NMP solvent at 90 °C under vacuum. X-ray diffraction (XRD, Rigaku Miniflex) was measured using Cu-Kα radiation (λ = 0.154 nm) in the 2θ range 10–80° to identify the crystallinity nature and phases. JSM-IT300HR In Touch Scope Scanning electron microscopy (SEM, JEOL USA, Inc.) was used to acquire the microstructure images and EDX maps. Transmission electron microscopy (TEM) images were acquired with JEOL 1400-PLUS at 120 kV field emission.¹³C and ²⁹Si Magic-angle spinning

(MAS) nuclear magnetic resonance (NMR) spectroscopy was performed with a Bruker Avance 500 MHz spectrometer at a magnetic field of 11.7 T, corresponding to resonance frequencies of 125.7 and 99.4 MHz, respectively. Spinning was performed in 2.5 mm rotors at 30 kHz. X-ray photoelectron spectroscopy (XPS) was done using the Kratos Axis Ultra (Kratos Analytical) at room temperature under 3.1 × 10⁻⁸ Pa using monochromatic Al source (14 kV and 8 mA) to record the core level atoms. The binding energies of all the elements were calibrated relative to C 1s at 284.8 eV.

Electrochemical measurements.—CR2032-type coin cells were assembled to evaluate the electrochemical performance of the anodes. The slurries were prepared with 90 wt% SiC/HC/Graphite or SiC/O/Graphite composite powder, 5 wt% C₆₅, and 5 wt% poly(vinylidene fluoride) (PVDF) binder. All powders were dried at 80 °C vacuum⁻¹ overnight and dry-mixed by mortar and pestle, which was then mixed with PVDF binder solution (5 wt% solution in NMP) and 1.5 g NMP in a 16 mL vial via low-energy ball milling (3 mm dia. yttria-stabilized zirconia media) overnight. The obtained slurries were then coated onto a copper foil (16 μm thick) using a wire-wound rod coater at a controlled speed of 50 mm s⁻¹. After drying at 80 °C vacuum^{-1/2} h, 18 mm dia. electrodes were punched out. The loading of active materials is ≈0.6 mg cm⁻².

Cells were assembled in an Ar-filled glovebox, with Li metal (16 mm × 600 μm, MTI Corp.) used as the counter electrode. Celgard 2400 (19 mm) was used as a separator, and 1.1 M LiPF₆ in EC:DC:DMC (1:1:1 weight ratio) with 10 wt% FEC additive as the electrolyte. A Bio-Logic SP-300 was used to measure the open-circuit voltage, the AC impedance, cyclic voltammetry (CV), and galvanostatic intermittent titration technique (GITT). The CV tests were conducted in the 0.01–3 V range with a scan rate of 0.5 mV s⁻¹. The galvanostatic intermittent titration technique (GITT) tests were applied to the half-cells between 0.01 – 3 V at a 0.1C rate for 10 min, followed by resting periods of 20 min. The potential change of the current pulse versus the square root of time (τ^{1/2}) exhibits linear behavior with R² of ≈ 0.89. The ion diffusion coefficient (D) was calculated per $D = \frac{4}{\pi} \left(\frac{n_M \times V_M}{A_e} \right)^2 \left(\frac{\Delta E_S}{\Delta E_T} \right)^2$ where n_M is the moles of active material, A_e is the contact area between the electrolyte and electrode, ΔE_S is the steady-state voltage change, and ΔE_T is the voltage change after eliminating the IR drop during the constant current pulse. The galvanostatic cycling of the half-cells was performed between 0.01 – 2.5 V vs Li/Li⁺ using a multi-channel Maccor test system. The applied current densities were calculated from 680 mAh g⁻¹ for SiC and 375 mAh g⁻¹ for graphite. Data shown in the article are the averages of three cells.

The half-cells after completing 250 cycles were decrimped in a dry room. The recovered electrodes were rinsed and soaked in DEC solvent to remove electrolyte salt residues that are not inherent to the SEI before dissolving the PVDF binder in NMP using ultrasonication. The electrodes were then dried overnight under vacuum at room temperature prior to the following characterization.



Scheme 1. Fabrication processes for SiC/HC with graphite composites.

Results and Discussion

Since distillative SiO₂ depolymerization methods were developed, our group has been continuously expanding the potential utility derived from silica-depleted RHA (SDRHA), including improving controllability of SiO₂:C ratios,⁴¹ which enables using RHA as a practical precursor for carbothermal reduction to solar-grade silicon (99.999% pure)⁴² or silicon non-oxide ceramics without adding external carbon sources;³³ high surface area fumed and precipitated silicas;⁴³ new precursors for solid Li⁺ electrolytes;³⁷ high-performance hybrid Li⁺ supercapacitors electrodes;³⁸ and the aforementioned potential intercalation-type anodes. Scheme 1 illustrates the SiC/HC/graphite composite fabrication process. In brief, SDRHA with appropriate SiO₂:C ratios was first synthesized by depolymerizing the SiO₂ in RHA for carbothermal reduction producing SiC/HC. The resulting SiC/HC was then blended with commercial spherical graphite by low-energy ball milling to fabricate SiC/HC/graphite composites.

Figure 1a presents the XRD patterns of SiC/HC before and after mixing with 30 wt% graphite (SiC/HC/30G). In addition to peaks assigned to 3C-SiC with stacking faults, the intense peak at $\approx 26.5^\circ$ 2θ can be indexed to the (0 0 2) plane of graphite, while peaks at $\approx 36^\circ$, 42° , 60° , and 72° 2θ are associated with diffraction from the (1 1 1), (2 0 0), (2 2 0), and (3 1 1) planes of 3C-SiC, respectively.

Pure spherical and elliptical graphite particles with diameters of $\approx 10 \mu\text{m}$ were explored as additives, of which the morphology is displayed in Fig. S1. After ball milling, the fibrous SiC whiskers and surrounding agglomerated SiC particles and hard carbon particles retain their morphologies found in as-prepared SDRHA-derived SiC, as seen in

Figure 1b. EDX imaging shows no distinct elemental Si areas in the composites, indicating SiC/HC is evenly distributed through the ball milling processes. The SiC structures investigated by TEM (Fig. 1c) show micrometer-sized spherical particles bridged by submicron-sized primary particles and whiskers.

The SiC/HC and SiC/O with/graphite composites were incorporated into half-cells to assess their electrochemical performance in Li storage. Figure 2a compares three CV scans of SiC/HC/30G graphite. In the initial cathodic scan, peaks in the 2–1.5 V range are ascribed to carbonate decomposition.

Peaks at $\approx 1\text{V}$ and $\approx 0.75\text{V}$ are attributed to SEI formation during the 1st cycle.^{19,44} As expected, the peak at $\approx 0.15\text{V}$ is associated with lithium intercalation into graphite forming LiC_x, while the two peaks at ≈ 0.19 and $\approx 0.25\text{V}$ in anodic scans originate from LiC_x.⁹ Meanwhile, SiC shows responses at higher potential at ≈ 0.9 and 1.2V in cathodic and anodic scans, respectively, consistent with that reported before.³⁴

Figure 2b shows representative charge and discharge profiles for the 1st and 250th cycle of SiC/HC/30G half-cells between 0.01–2.5 V. In agreement with the CV results, the plateaus that

appear between 0.25–0.01 V vs Li/Li⁺ are ascribed to intercalation of Li⁺ into graphite.⁹ In addition, SiC/HC and SiC/O contribute to lithiation between 0.9–0.25 V (Fig. S2), corresponding to increases shown in the curves. Apparently, the typical charge and discharge curves are a superposition of the two components; thus, the presence of SiC improves Li⁺ capacities in the higher potential window for the composite anodes. Meanwhile, $>80\%$ capacities are obtained during charge and discharge at 0.01–0.2 V, compatible with LiPF₆ dissolved in EC:DMC mixture electrolyte, of which the SEI layer formation takes place mostly within 0.2–1.0 V vs Li/Li⁺.⁴⁵ This ensures the feasibility of using SiC/HC or SiC/O with graphite composites as anodes and represents an important factor in determining the long-term cycling performance of Li⁺ batteries.

Moreover, capacity increments on extended cycling highlight the performance of SiC as an anode compared to other materials. Here, the SiC/HC/graphite or SiC/O/graphite composites retain their properties. Both lithiation and delithiation curves for their composite electrodes show enhanced capacities at the cut-off voltage at the 250th cycle compared to the 1st cycle (Fig. 2b). Figure 2c shows specific capacities during galvanostatic cycling and provides a better illustration of capacity improvements with time.

SiC/HC/30G half-cells show specific capacities increase from 420 to 480 mAh g⁻¹ after 20 cycles at C/2. At 1C, the specific capacities improve from ≈ 280 to ≈ 360 mAh g⁻¹ after 40 cycles. When the C rate is increased to 2C, the specific capacities remain at ≈ 220 mAh g⁻¹. The less evident capacity changes at higher C rates are consistent with previous observations with pristine SiC/HC, while the SiC/HC solely delivers 200 mAh g⁻¹ under the same charge/discharge condition at 2C. Cycling at C/10 leads to prominent capacity increases, with specific discharge capacities increasing from ≈ 750 to ≈ 950 mAh g⁻¹ over 150 cycles. With pristine SiC/HC, achieving the same capacities (≈ 950 mAh g⁻¹) from ≈ 500 mAh g⁻¹ takes 550 cycles at C/10, as seen in Fig. S3. Thus, the SiC/HC/30G doubles the rate increases, saving $>70\%$ time to reach the specific capacities competitive with porous Si-based anodes,^{46–48} making RHA-derived SiC a more practical alternate anode material.

As for SiC/O/30G half-cells charged/discharged following the same protocols, the specific capacities increase from ≈ 350 to ≈ 390 mAh g⁻¹ and ≈ 270 to 350 mAh g⁻¹ at C/2 and 1C, respectively. The specific capacities of SiC/O/30G at 2C remain at ≈ 190 mAh g⁻¹, ≈ 10 mAh g⁻¹ higher than SiC/O. Cycling at C/10 for 150 cycles results in increases from ≈ 500 to ≈ 600 mAh g⁻¹, corresponding to $>50\%$ faster rate increases. Furthermore, graphite half-cells prepared using the same procedures exhibit typical performance,⁹ where the specific discharge capacities remained ≈ 370 mAh g⁻¹, ≈ 280 mAh g⁻¹, and ≈ 170 mAh g⁻¹ at C/10, C/2 and 1C, respectively. As expected, no capacity increases are observed with pure graphite. At 2C, the capacities decrease rapidly

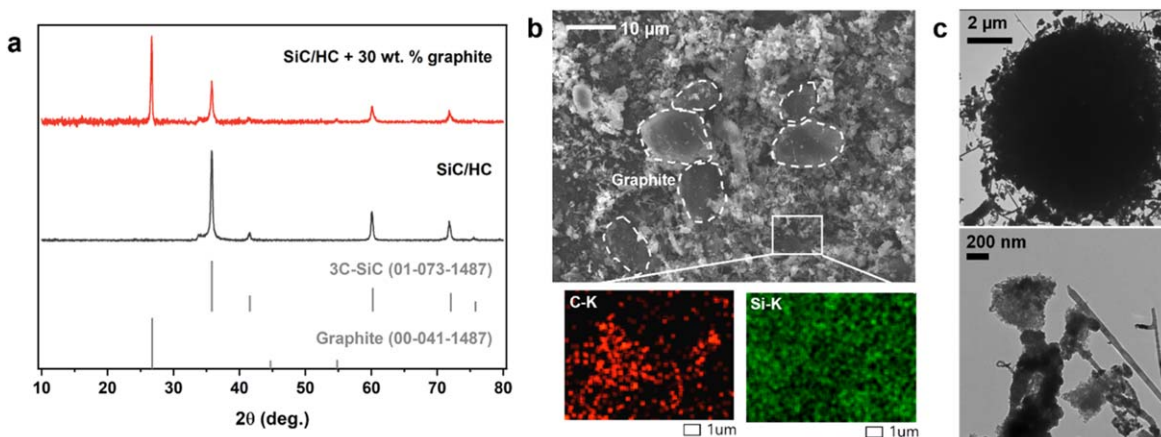


Figure 1. (a). XRD, (b). SEM/EDX of SiC/HC/30G powders, and (c). TEM of agglomerated SiC in the SiC/HC/30G composite powder.

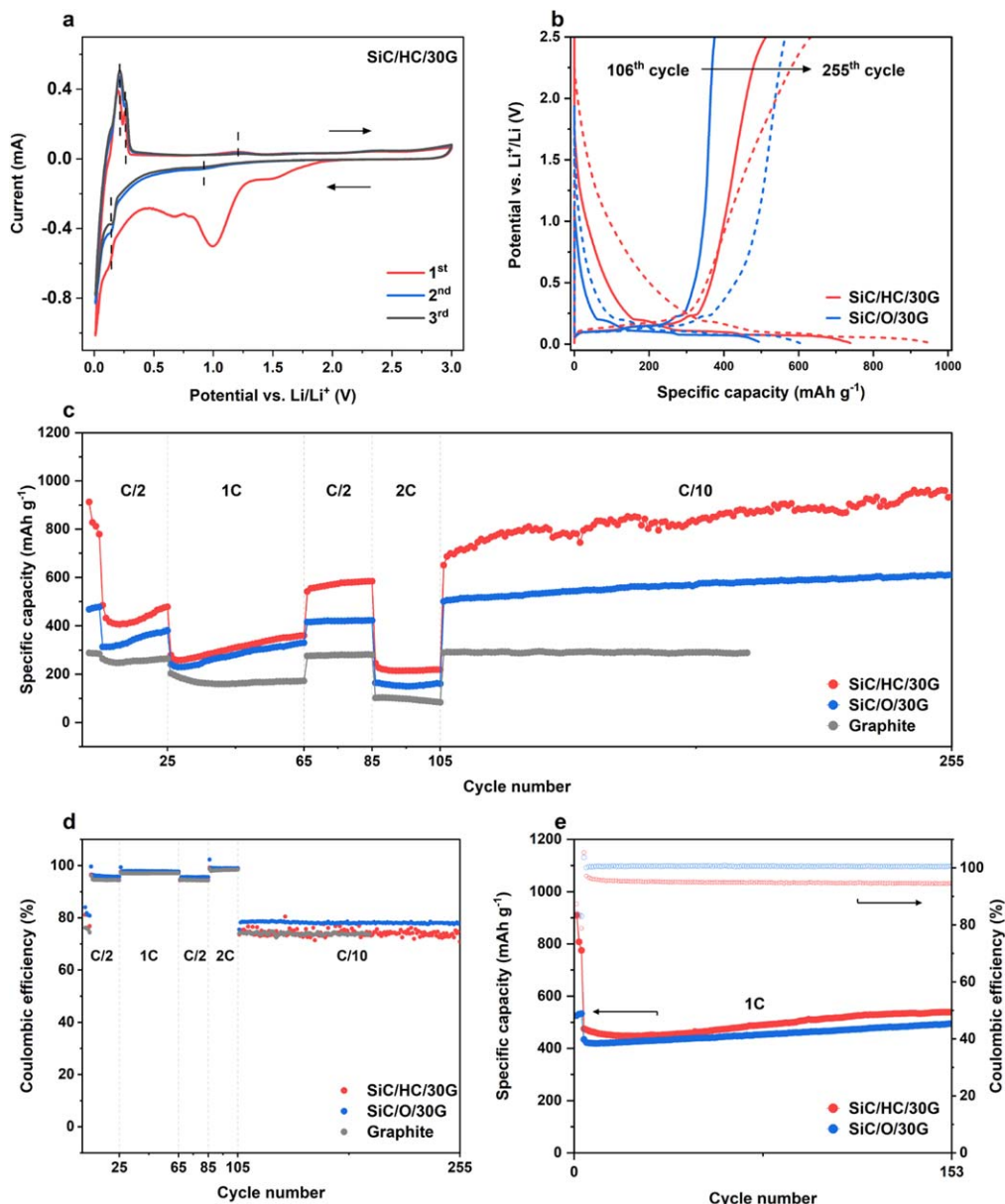


Figure 2. (a). CV curves of SiC/HC/30G half-cells between 0.01–3 V at 0.5 mV s^{-1} ; (b). charge/discharge curves of 106th (solid line) and 255th (dashed line) cycle at C/10; (c). cycling performance of 255 cycles; (d). the corresponding Coulombic efficiency at C/10, C/2, 1C and 2C; and (e). cycling performance at 1C for 150 cycles of SiC/HC/30G and SiC/O/30G (first 3 cycles at C/10 to form a stable SEI).

to $\approx 80 \text{ mAh g}^{-1}$ after 20 cycles, demonstrating the consensus that graphite anodes are the limiting factor for fast charging.^{49,50}

The Coulombic efficiencies (CE) of the cells mentioned above are illustrated in Fig. 2d. Yet the initial Coulombic efficiency (ICE) is only $\approx 60\%$ due to the high surface area SiC/HC nanocomposites and consequent large irreversible Li^+ consumption,³⁴ it was found that the capacity retention of SiC/HC/30G at the 106th cycle is $\approx 96\%$ compared to the 2nd cycle (Fig. S4), both at C/10. Benefits from the capacity increases, the retention approaches $>120\%$ after another 150 cycles. As for SiC/O/30G, the capacity retention after 150 cycles at C/10 stabilizes at $\approx 93\%$. The CEs for SiC/HC/30G and SiC/O/30G are $\approx 97\%$ at C/2, $>99\%$ at 1C, and $>99\%$ at 2C.

However, one may question the relatively low CEs at C/10 for SiC/HC/30G ($\approx 75\%$) and SiC/O/30G ($\approx 80\%$). As stated above, a half-cell configuration was chosen to offer fundamental electrochemical insights during the early-stage studies, where the different SiC electrodes were paired against Li-metal counter electrodes and tested with excess electrolyte.⁵¹ In such half-cells, the CE is not an ideal

indicator for the actual cycling performance of those materials in full Li^+ batteries.^{52,53} Nonetheless, it is worth noting here that gaps between charge and discharge capacities are also shown in the graphite half-cells under the test conditions used, suggesting a large portion of the discrepancies between charge and discharge may be attributable to parasitic reactions, including electrode material surface properties, induced Li dendrite growth, or the cycling parameters.^{54,55}

Meanwhile, it is also observed that the presence of HC generally results in $\approx 5\%$ lower CE in SiC/O anodes, which is more evident in Fig. 2e when continuously charging/discharging the samples at 1C for 150 cycles. The SiC/HC/30G half-cells show specific discharge capacities increasing from $\approx 450 \text{ mAh g}^{-1}$ and $\approx 560 \text{ mAh g}^{-1}$, with CE maintained at $\approx 95\%$, while those for SiC/O/30G half-cells increase from $\approx 400 \text{ mAh g}^{-1}$ and $\approx 490 \text{ mAh g}^{-1}$ with CEs $>99\%$.

It has been demonstrated that low CE remains the primary obstacle to address for practical application of HC anodes. In particular, the high HC specific surface area consumes excessive

amounts of electrolyte, and heteroatoms at graphene layer structures both contribute to trapping Li^+ irreversibly or alkali metal ions in the HC matrix.^{56,57} Nevertheless, those inherent structural properties also result in smaller ionic transfer distances, enabling fast capacitive ion storage.^{58,59} This is also reflected in the SiC/HC/30G composites, as discussed above.

As such, the ratio of SiC/HC to graphite within the composites must be optimized to balance between reversible capacities, capacity rate increases, and rate capabilities. SiC/HC/30G and SiC/O/30G were selected as they showed more promising electrochemical performance while keeping the graphite amount in accord with the sustainable perspectives of agricultural waste-derived materials. However, investigating the performance of composites with various ratios provides insights into understanding the interaction between components. Figure 3a illustrates the galvanostatic cycling performance of SiC/HC + 10 wt% graphite (SiC/HC/10G) and SiC/O + 10 wt% graphite (SiC/O/10G). Specific capacities for SiC/HC/10G are ≈ 400 , ≈ 390 , and ≈ 215 mAh g^{-1} at C/2, 1C, and 2C, respectively, whereas for SiC/O/10G they are ≈ 380 , ≈ 310 , and ≈ 170 mAh g^{-1} at C/2, 1C, and 2C, respectively.

The differential capacity (dQ/dV) profiles from the 2nd cycle of the half-cells in Figs. 3b and 3c provide more in-depth analyses of the reaction mechanisms of the composite electrodes with different ratios. The dQ/dV profiles were normalized by graphite mass such that graphite Li^+ intercalation and deintercalation peaks at 0.2, 0.1, and 0.07 V vs Li/Li^+ , and at 0.23, 0.1, and 0.15 V vs Li/Li^+ , respectively, were used as indicators of the composite interaction effects. In SiC/HC/10G and SiC/O/10G half-cells, the featured peak locations shift to higher voltage during charge and lower voltage during discharge. In addition, these peaks generally reduce in magnitude and become broader in composites compared to pristine

graphite, suggesting the SiC/HC or SiC/O with 10 wt% graphite hindered graphite from complete lithiation/delithiation, presumably due to significant resistive and diffusion polarization effects at graphite in the composite electrodes.^{60,61} In contrast, the SiC/HC/30G and SiC/O/30G show less evident peak changes and more intense responses than graphite, suggesting less localized polarization and that SiC components probably facilitate graphite lithiation/delithiation processes. At present, these effects remain to be identified.

The Li^+ diffusion coefficients calculated from the galvanostatic intermittent titration technique (GITT) for SiC/HC/30G as a function of the state of charge (SOC) are illustrated in Fig. 3d. It is seen that Li^+ diffusion coefficients are 10^{-16} – 10^{-14} $\text{cm}^2 \text{s}^{-1}$, while those for SiC/HC half-cells are 10^{-18} – 10^{-16} $\text{cm}^2 \text{s}^{-1}$.³⁴ The trends between charge and discharge are nearly identical. During discharge, the initial diffusion coefficients are $\approx 10^{-12}$ $\text{cm}^2 \text{s}^{-1}$, increasing to $\approx 10^{-9}$ $\text{cm}^2 \text{s}^{-1}$ at $\approx 10\%$ SOC. Then, the diffusion coefficients gradually decreased to $\approx 10^{-13}$ $\text{cm}^2 \text{s}^{-1}$ at SOC $\approx 15\%$, followed by increasing to $\approx 10^{-11}$ $\text{cm}^2 \text{s}^{-1}$ at SOC $\approx 20\%$. The fluctuations of Li^+ diffusion coefficients originate from phase transformations that occur in SiC and/or graphite. It was reported that significant increases in spacing (0.1 Å) provide sufficient space for Li^+ diffusion, subsequently leading to increased diffusion coefficients.^{62,63} Thereafter, the Li^+ diffusion coefficients decrease to $\approx 10^{-15}$ $\text{cm}^2 \text{s}^{-1}$ on further charging/discharging, attributed to the increased Li^+ concentrations in the anode and possible formation of intermediate phases that hinder Li^+ transport.⁶⁴

To gain a better understanding of the composite anodes' working and aging mechanisms, post-mortem analyses were conducted after the above discussed 250-cycle galvanostatic cycling tests. The cycled SiC/HC/30G and SiC/O/30G half-cells were de-crimped by

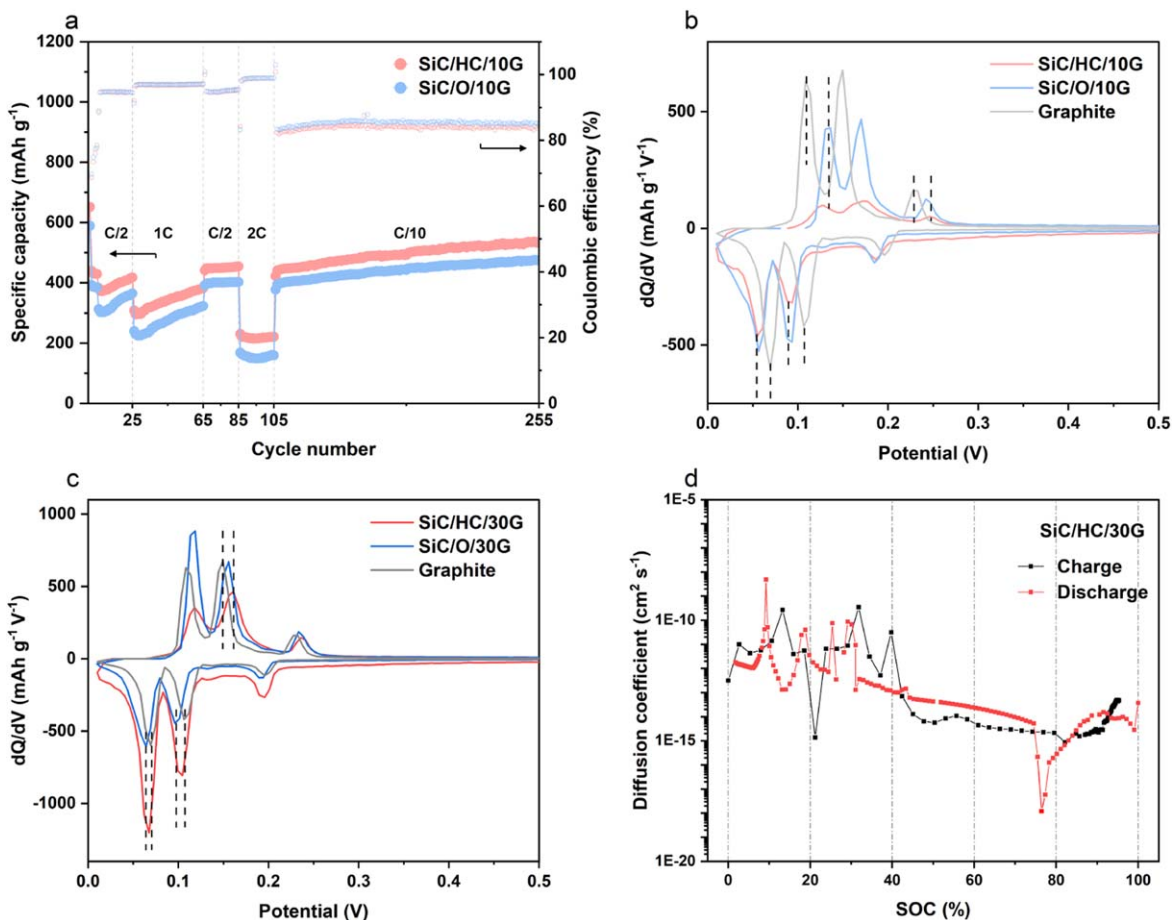


Figure 3. (a). Cycling performance of SiC/HC/10G and SiC/O/10G at C/10, C/2, 1C and 2C; the 2nd cycle differential capacity (dQ/dV) profiles of (b). SiC/HC/10G and SiC/O/10G, and (c). SiC/HC/30G and SiC/O/30G; (d). Li^+ diffusion coefficients of SiC/HC/30G measured by GITT.

the methods described in the experimental section. Figure 4a illustrates the XRD of SiC/HC/30G electrode after 250 cycles. Compared with the pristine composites shown in Fig. 1a, peaks indexed to graphite and 3C-SiC are still observed. Additional weak peaks at $\approx 38^\circ$, 41° , 64° 2θ are attributed to (1 0 3), (1 0 4), (1 0 9) planes of 6H-SiC. Doublet peaks at $\approx 48^\circ$ and 49° 2θ can be assigned to lithiated graphite (LiC_x), indicating residual lithium insertion into graphite layers.⁸

^{13}C and ^{29}Si MAS NMR spectroscopy was used to further probe structural changes in the composites with graphite. The ^{13}C spectra of pristine and cycled SiC/HC/30G in Fig. 4b are dominated by broad C=C units (sp^2 carbon) peaks. Spectral deconvolution indicates at least two resolved signals at 140 and 220 ppm, corresponding to graphite and HC in the composites, respectively.^{65,66} In the cycled composites (recovered after discharging to 2.5 V), both peaks show slight broadening and shifts to lower values of 110 and 190 ppm, respectively. The downfield shifts indicate incomplete Li deintercalation with some Li^+ residue in the composites, consistent with the XRD results and the observed CE discussed above. Meanwhile, peaks for SiC, usually centered at $-15 \sim -23$ ppm are absent in the ^{13}C spectra. Vyalikh et al.⁶⁷ subjected possible unobservable ^{13}C spins in MAS NMR to the reduced resolution in low sample volume and demagnetizing fields within graphitic regions.⁶⁸

In contrast to the single -16.5 ppm ^{29}Si NMR peak for cubic SiC observed in pristine SiC/HC, a second broad peak centered around -34 ppm is present in the SiC/HC/30G composites (Fig. 4c). The latter peak hints at mixed C/O environments around Si. This unexpected phenomenon can be understood first from the experimental material preparation method, by which the SiC components may be partially oxidized during ball-milling with graphite in the solvent. It has been reported that SiC oxidizes at comparatively lower temperatures with smaller particle sizes, with nanosized material showing an oxidation activation energy of ≈ 80 kJ mol $^{-1}$.⁶⁷ On the other hand, introducing conductive graphite also induces demagnetizing local fields that generally result in a mismatch and broadening or even quenching of the resonance signals.^{69,70} Nonetheless, Li insertion minimizes the demagnetizing effects and enhances field homogeneity, resulting in improved NMR spectral resolution.⁶⁸ Therefore, in the cycled ^{29}Si spectra, the narrower peak shifts to lower ppm and deconvoluted to reveal a peak at -8.3 ppm for irreversible Li_xSiC and a peak at -21 ppm for hexagonal SiC, agreeing well with the pristine SiC/HC systems.⁷¹

Figure 5 SEM images reveal the morphologies of SiC/HC/30G and SiC/O/30G before and after cycling. As expected, the electrode surfaces are covered with SEI layers after cycling. Nonetheless, SiC whiskers are still visible, indicating that the SEI is not excessively thick even with the high SiC/HC surface areas (>200 m 2 g $^{-1}$) and SiC/O (>40 m 2 g $^{-1}$) components.

The synergistic effects of mixed components lead to electrodes consisting of multiple interfaces, improving stress relaxation and

mechanical stability.⁷² This also demonstrates that the SEI layers on the composite electrodes are robust and stable, suppressing deleterious Li^+ loss and rise in the charge transfer resistance and interface impedances,^{73,74} which could be anticipated to correlate with the long-term cycling performance of the composite electrodes. Moreover, the cycled electrodes retain integrity with no cracking observed from the top view or volume changes from the cross-section view, ensuring the fundamental precondition for the cyclabilities of the composite electrodes.

Surface elemental analyses of the SiC/HC/30G and SiC/O/30G electrodes before and after cycling are shown in Fig. 6. Within XPS analyses, at depths of ≈ 10 nm, F, O, C, and Si elements were found in all electrode samples. Figure 6a presents the deconvoluted C 1s spectra of the SiC/HC/30G and SiC/O/30G electrodes before and after cycling. The pristine electrodes show C-Si bonds at ≈ 283 eV. The prominent peak at 284 eV is ascribed to sp^2 C-C, and that at 285 eV to sp^3 C-C overlap with C-O from carbon components (HC, graphite, C_{65}). The peak at ≈ 289 eV is assigned to F-C-H and F-C-F species from the PVDF binder.⁷⁵ After cycling, peaks for lithiated graphite species Li_xC_6 and/or lithium carbide (Li_2C_2) are detected at 282–283 eV,^{76,77} consistent with the XRD results. The C-C peaks are broader due to carbonate decomposition. Specifically, both EC and DMC decomposition release C-H species at ≈ 284.6 eV, while Li_2CO_3 and metastable alkyl lithium carbonates ROCO_2Li show signals at ≈ 289.5 and ≈ 291 eV, respectively.⁷⁸

The Si 2p spectra in Fig. 6b are similar to those of SiC/HC and SiC/O without graphite.⁷¹ The intense peak at ≈ 103 eV is from the oxidized SiC surface, forming C-Si-O/Si-C-O and O-Si-O.⁷⁹ After cycling, the Si-C peaks at ≈ 101 eV shift slightly to lower binding energies due to Li incorporation. As previously reported,⁷¹ conversion and alloying are not prominent lithiation mechanisms for SiC anodes; thus, no elemental Si (≈ 99.5 eV) or Li_xSi (≈ 95 – 97 eV) components are observed in the spectra.

As expected, the F1s XPS spectrum shown in Fig. 6c indicates the main PVDF component in pristine electrodes. On deconvolution, the F-C-F peak appears at ≈ 685.5 eV, along with a peak at ≈ 684.5 eV associated with H-C-F.⁷⁵ Note that the convoluted peaks for the pristine SiC/O/30G electrodes appear at higher binding energy, probably induced by surface interfacial interactions between PVDF H-C-F dipoles and oxygen on the SiC/O surface that shows higher electronegativity. The peak at ≈ 684.5 eV broadens and is more intense after cycling due to decomposition products from LiPF_6 , e.g. LiF and $\text{Li}_x\text{PF}_y\text{O}_z$.⁸⁰ The Li 1s spectra (Fig. 6d) present intense peaks for formation of irreversible $\text{Li}_x\text{Si}_y\text{C}$ and LiF species in the SEI. Distinctive peaks corresponding to the Li_xC components from lithiated graphite are in agreement with the C 1s spectra, XRD, and ^{13}C MAS NMR results discussed above.

Conclusions

SDRHA-sourced SiC offers potential as an alternate anode that delivers competitive specific capacities and eliminates the structural

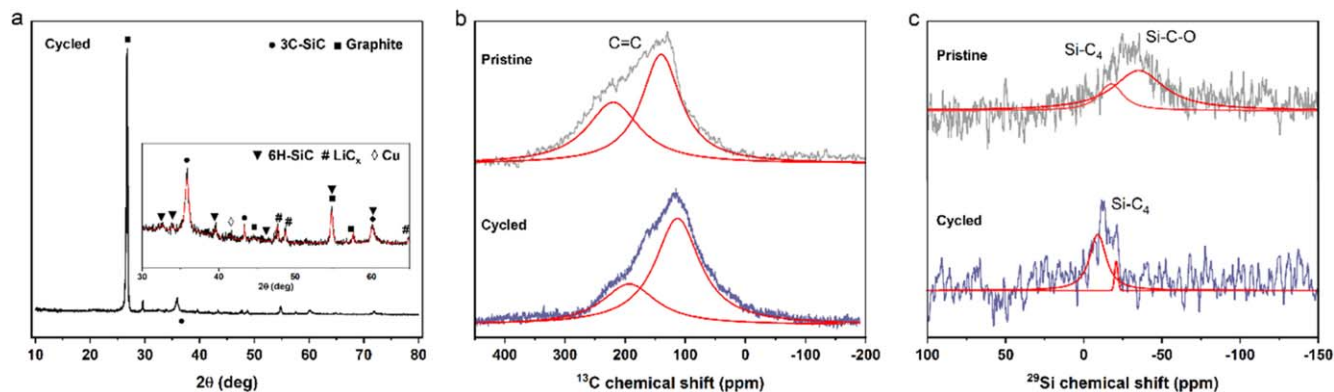


Figure 4. (a). XRD, (b). ^{13}C and (c). ^{29}Si MAS NMR spectra of pristine SiC/HC/30G powder and cycled (250 cycles) electrode.

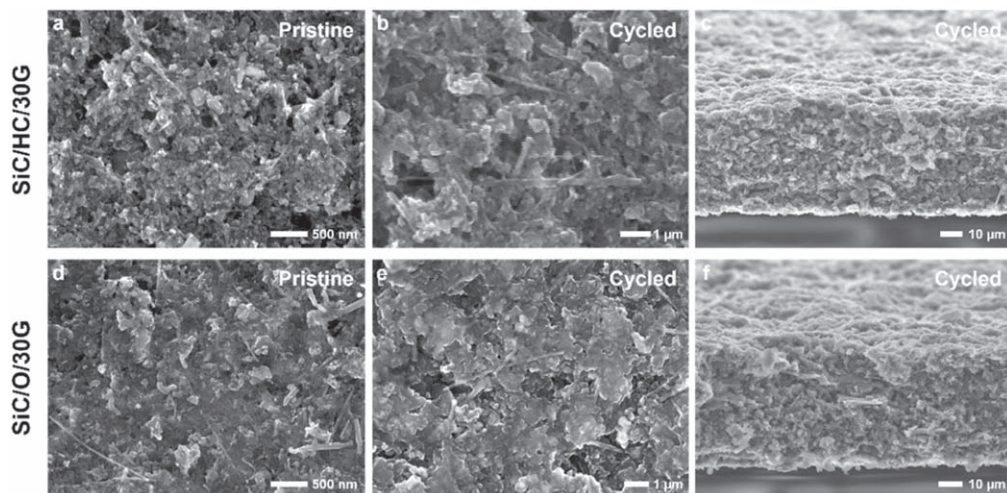


Figure 5. SEM images of (a). pristine and cycled (250 cycles) (b). top view, (c). cross-section of SiC/HC/30G electrodes; and (d). pristine and cycled (250 cycles) (e). top view, (f). cross-section of SiC/O/30G electrodes.

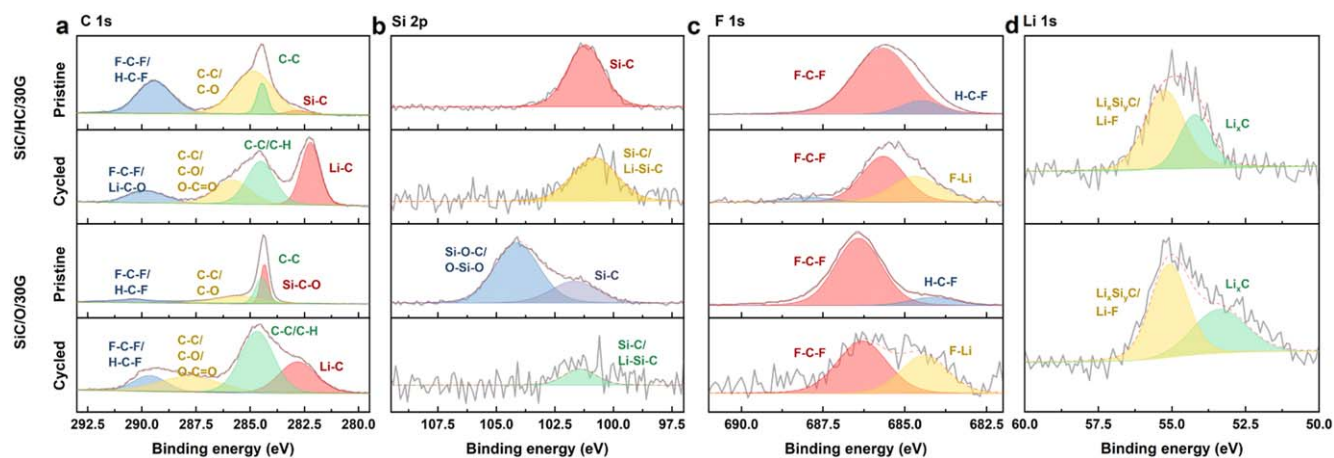


Figure 6. (a). C 1s, and (b). Si 2p, (c). F 1s, core spectra of pristine and cycled (250 cycles) SiC/HC/30G and SiC/O/30G electrodes, and (d). Li 1s core spectra of the corresponding cycled electrodes (250 cycles).

change obstacles found for silicon metal anodes. SiC/graphite composites were designed and fabricated to promote performance. Adding small amounts of graphite to SiC/HC composites still results in extraordinary sustainability compared to the environmentally harmful graphite production but boosts the performance by doubling rates of capacity increase. The optimized graphite content was found to be 30 wt% to address graphite diffusion polarization effects and balance various electrochemical performance indices for the composite electrodes.

The specific discharge capacities of SiC/HC/30G reach ≈ 950 mAh g^{-1} over 150 cycles at C/10, which saves $>70\%$ time to reach the specific capacities found for pristine SiC/HC and enables more practical composites as alternatives to Si anodes. Detailed analyses of SiC/O/30G composites demonstrate that the coincidentally formed HC also facilitates anode performance in the composites with graphite. The high surface areas and inherent structural properties of HC result in relatively lower CE shown in the half-cell configuration; the shorter ionic transfer distance also promotes the fast capacitive Li^+ storage performance.

Moreover, post-mortem analyses provide a glance at interactions within the SiC/HC/graphite composites. XRD reveals partial cubic to hexagonal SiC phase changes, while lithiated graphite was observed to form from XRD and XPS measurements. ^{13}C MAS NMR suggests demagnetizing local field effects from the conductive graphite, while the enhanced resolution after cycling also proves

residual Li in the graphite layers. Consistent with the previously observed cubic to hexagonal SiC phase transition on charging/discharging, the same phenomenon was also demonstrated by XRD and ^{29}Si MAS NMR, explaining the capacity increments. The SEIs observed by SEM are rather thin after long-term cycling, even with the high surface areas of the SiC/HC and SiC/O components, indicating that the synergistic effect of multiple component interfaces improves stress relaxation and mechanical stability. The robustness of the composite electrodes allows maintenance of structural integrity during cycling and shows minimal volume expansion, as expected.

Acknowledgments

We acknowledge supports from DMR NSF Grant No. DMR-1926199 and a generous gift from Mercedes-Benz Research & Development North America (MBRDNA) for this work. We appreciate the technical support from the University of Michigan Battery Lab, Van Vlack lab and Michigan Center for Materials Characterization. We also thank Wadham Energy Inc. for supplying the rice hull ash for our research.

ORCID

Richard M. Laine  <https://orcid.org/0000-0003-4939-3514>

References

- X. Lan, P. Tans, and K. W. Thoning, Version (2023-05) "Trends in globally-averaged CO₂ determined from NOAA Global Monitoring Laboratory measurements".
- U.S. Environmental Protection Agency, *EPS (2022) Inventory of U.S. Greenhouse Gas Emissions and Sinks: 1990-2020EPA 430-R-22-003* (2022).
- Y. Ding, Z. P. Cano, A. Yu, J. Lu, and Z. Chen, *Electrochem. Energy Rev.*, **2**, 1 (2019).
- R. Schmich, R. Wagner, G. Hörpel, T. Placke, and M. Winter, *Nat. Energy*, **3**, 267 (2018).
- J. Moon et al., *Nat. Commun.*, **12**, 2714 (2021).
- J.-I. Lee, E.-H. Lee, J.-H. Park, S. Park, and S.-Y. Lee, *Adv. Energy Mater.*, **4**, 1301542 (2014).
- D. Larcher and J.-M. Tarascon, *Nat. Chem.*, **7**, 19 (2015).
- M. Drüe, M. Seyring, and M. Rettenmayr, *J. Power Sources*, **353**, 58 (2017).
- J. Asenbauer, T. Eisenmann, M. Kuenzel, A. Kazzazi, Z. Chen, and D. Bresser, *Sustain. Energy Fuels*, **4**, 5387 (2020).
- C. Fan, H. He, K. Zhang, and S. Han, *Electrochim. Acta*, **75**, 311 (2012).
- D. Aurbach, H. Teller, M. Koltypin, and E. Levi, *J. Power Sources*, **119–121**, 2 (2003).
- S. Schweidler, L. de Biasi, A. Schiele, P. Hartmann, T. Brezesinski, and J. Janek, *J. Phys. Chem. C*, **122**, 8829 (2018).
- G. G. Eshetu, H. Zhang, X. Judez, H. Adenusi, M. Armand, S. Passerini, and E. Figgemeier, *Nat. Commun.*, **12**, 5459 (2021).
- X. Zhao and V.-P. Lehto, *Nanotechnology*, **32**, 042002 (2020).
- B. A. Boukamp, G. C. Lesh, and R. A. Huggins, *J. Electrochem. Soc.*, **128**, 725 (1981).
- A. Franco Gonzalez, N.-H. Yang, and R.-S. Liu, *J. Phys. Chem. C*, **121**, 27775 (2017).
- J. P. Pender et al., *ACS Nano*, **14**, 1243 (2020).
- J. R. Szczech and S. Jin, *Energy Environ. Sci.*, **4**, 56 (2011).
- C. Xu, F. Lindgren, B. Philippe, M. Gorgoi, F. Björefors, K. Edström, and T. Gustafsson, *Chem. Mater.*, **27**, 2591 (2015).
- A. L. Michan et al., *Chem. Mater.*, **28**, 8149 (2016).
- J. Xu et al., *Nano Lett.*, **22**, 3054 (2022).
- W. Tu, Z. Bai, Z. Deng, H. Zhang, and H. Tang, *Nanomaterials*, **9**, 432 (2019).
- W. An et al., *ACS Appl. Mater. Interfaces*, **14**, 10308 (2022).
- Y. Lu, P. Chang, L. Wang, J. Nzabihimana, and X. Hu, *Funct. Mater. Lett.*, **12**, 1850094 (2019).
- R. Yi, F. Dai, M. L. Gordin, S. Chen, and D. Wang, *Adv. Energy Mater.*, **3**, 295 (2013).
- X. Zhao, N. Kalidas, and V.-P. Lehto, *J. Power Sources*, **529**, 231269 (2022).
- F. Jeschull and S. Trabesinger, *Batter. Supercaps*, **4**, 131 (2021).
- H. J. Kwon, J.-Y. Hwang, H.-J. Shin, M.-G. Jeong, K. Y. Chung, Y.-K. Sun, and H.-G. Jung, *Nano Lett.*, **20**, 625 (2020).
- H. Wu, L. Zheng, N. Du, B. Sun, J. Ma, Y. Jiang, J. Gong, H. Chen, and L. Wang, *ACS Appl. Mater. Interfaces*, **13**, 22323 (2021).
- S. He, S. Huang, S. Wang, I. Mizota, X. Liu, and X. Hou, *Energy Fuels*, **35**, 944 (2021).
- C. Heubner, T. Liebmann, O. Lohrberg, S. Cangaz, S. Maletti, and A. Michaelis, *Batter. Supercaps*, **5**, e202100182 (2022).
- S. Chae, S.-H. Choi, N. Kim, J. Sung, and J. Cho, *Angew. Chem. Int. Ed.*, **59**, 110 (2020).
- M. Yu, E. Temeche, S. Indris, and R. M. Laine, *Green Chem.*, **23**, 7751 (2021).
- M. Yu, E. Temeche, S. Indris, W. Lai, and R. M. Laine, *Green Chem.*, **24**, 4061 (2022).
- N. A. Banek, D. T. Abele, K. R. McKenzie Jr, and M. J. Wagner, *ACS Sustain. Chem. Eng.*, **6**, 13199 (2018).
- A. D. Jara, A. Betemariam, G. Woldetinsae, and J. Y. Kim, *Int. J. Min. Sci. Technol.*, **29**, 671 (2019).
- X. Zhang, E. Temeche, and R. M. Laine, *Green Chem.*, **22**, 7491 (2020).
- E. Temeche, M. Yu, and R. M. Laine, *Green Chem.*, **22**, 4656 (2020).
- P. Li, H. Kim, S.-T. Myung, and Y.-K. Sun, *Energy Storage Mater.*, **35**, 550 (2021).
- N. S. Hochgatterer, M. R. Schweiger, S. Koller, P. R. Raimann, T. Wöhrle, C. Wurm, and M. Winter, *Electrochem. Solid-State Lett.*, **11**, A76 (2008).
- R. M. Laine, J. C. Furgal, P. Doan, D. Pan, V. Popova, and X. Zhang, *Angew. Chem.*, **128**, 1077 (2016).
- J. C. Marchal, D. J. K. Iii, P. McDonnell, K. Sun, and R. M. Laine, *Green Chem.*, **17**, 3931 (2015).
- C.-D. Li, M.-U. Saeed, N. Pan, Z.-F. Chen, and T.-Z. Xu, *Mater. Des.*, **107**, 440 (2016).
- Y. Yang, Z. Wang, G. Yan, H. Guo, J. Wang, X. Li, Y. Zhou, and R. Zhou, *Ceram. Int.*, **43**, 8590 (2017).
- S. J. An, J. Li, C. Daniel, D. Mohanty, S. Nagpure, and D. L. Wood, *Carbon*, **105**, 52 (2016).
- J. Tang et al., *Nanoscale*, **11**, 10984 (2019).
- W. An, B. Gao, S. Mei, B. Xiang, J. Fu, L. Wang, Q. Zhang, P. K. Chu, and K. Huo, *Nat. Commun.*, **10**, 1447 (2019).
- J. Ma, H. Zhang, R. Liu, W. Zhang, S. Han, J. Han, G. Xu, L. Li, Y.-S. He, and Z.-F. Ma, *Sci. China Mater.*, **66**, 493 (2023).
- Q. Liu, C. Du, B. Shen, P. Zuo, X. Cheng, Y. Ma, G. Yin, and Y. Gao, *RSC Adv.*, **6**, 88683 (2016).
- C. Mao, R. E. Ruther, J. Li, Z. Du, and I. Belharouak, *Electrochem. Commun.*, **97**, 37 (2018).
- J. Liu, J. Wang, C. Xu, H. Jiang, C. Li, L. Zhang, J. Lin, and Z. X. Shen, *Adv. Sci.*, **5**, 1700322 (2018).
- J. Xiao et al., *Nat. Energy*, **5**, 561 (2020).
- M. C. Schulze and N. R. Neale, *ACS Energy Lett.*, **6**, 1082 (2021).
- C. Fang et al., *Nature*, **572**, 511 (2019).
- P. Albertus, S. Babinec, S. Litzelman, and A. Newman, *Nat. Energy*, **3**, 16 (2018).
- Y. Rangom, R. R. Gaddam, T. T. Duignan, and X. S. Zhao, *ACS Appl. Mater. Interfaces*, **11**, 34796 (2019).
- F. Béguin, F. Chevallerier, C. Vix-Guterl, S. Saadallah, V. Bertagna, J. N. Rouzaud, and E. Frackowiak, *Carbon*, **43**, 2160 (2005).
- H. Zheng, Q. Qu, L. Zhang, G. Liu, and V. S. Battaglia, *RSC Adv.*, **2**, 4904 (2012).
- L.-F. Zhao, Z. Hu, W.-H. Lai, Y. Tao, J. Peng, Z.-C. Miao, Y.-X. Wang, S.-L. Chou, H.-K. Liu, and S.-X. Dou, *Adv. Energy Mater.*, **11**, 2002704 (2021).
- A. Fly and R. Chen, *J. Energy Storage*, **29**, 101329 (2020).
- M. Huang, *Batteries*, **5**, 59 (2019).
- D. Allart, M. Montaru, and H. Gualous, *J. Electrochem. Soc.*, **165**, A380 (2018).
- T. Ohzuku, Y. Iwakoshi, and K. Sawai, *J. Electrochem. Soc.*, **140**, 2490 (1993).
- J. H. Park, H. Yoon, Y. Cho, and C.-Y. Yoo, *Materials*, **14**, 4683 (2021).
- Y. Maniwa, M. Sato, K. Kume, M. E. Kozlov, and M. Tokumoto, *Carbon*, **34**, 1287 (1996).
- J. Conard, H. Estrade, P. Lauginie, H. Fuzellier, G. Furdin, and R. Vasse, *Phys. BC*, **99**, 521 (1980).
- G. Ervin Jr, *J. Am. Ceram. Soc.*, **41**, 347 (1958).
- A. Vyalikh, V. O. Koroteev, W. Münchgesang, T. Köhler, C. Röder, E. Brendler, A. V. Okotrub, L. G. Bulusheva, and D. C. Meyer, *ACS Appl. Mater. Interfaces*, **11**, 9291 (2019).
- R. Alcántara, F. J. Fernández Madrigal, P. Lavela, J. L. Tirado, J. M. Jiménez Mateos, R. Stoyanova, and E. Zhecheva, *Chem. Mater.*, **11**, 52 (1999).
- R. Alcántara, G. F. Ortiz, P. Lavela, J. L. Tirado, R. Stoyanova, and E. Zhecheva, *Chem. Mater.*, **18**, 2293 (2006).
- M. Yu, E. Temeche, S. Indris, W. Lai, and R. M. Laine, *Green Chem.*, **24**, 4061 (2022).
- N. Sharma, D. Puthusseri, M. O. Thotiyl, and S. Ogale, *ACS Omega*, **2**, 8818 (2017).
- M. Broussely, S. Herreyre, P. Biensan, P. Kasztelna, K. Nechev, and R. J. Staniewicz, *J. Power Sources*, **97–98**, 13 (2001).
- D. Zhang, B. S. Haran, A. Durairajan, R. E. White, Y. Podrazhansky, and B. N. Popov, *J. Power Sources*, **91**, 122 (2000).
- P. Viswanath and M. Yoshimura, *SN Appl. Sci.*, **1**, 1519 (2019).
- S. Malmgren, K. Ciosek, R. Lindblad, S. Plogmaker, J. Kühn, H. Rensmo, K. Edström, and M. Hahlin, *Electrochim. Acta*, **105**, 83 (2013).
- B. Philippe, M. Hahlin, K. Edström, T. Gustafsson, H. Siegbahn, and H. Rensmo, *J. Electrochem. Soc.*, **163**, A178 (2015).
- A. Moretti, V. Sharova, D. V. Carvalho, A. Boulineau, W. Porcher, I. de Meatz, and S. Passerini, *Batter. Supercaps*, **2**, 240 (2019).
- W. Lu, A. T. Tarekne, Y. Ou, S. Kamiyama, and H. Ou, *Sci. Rep.*, **9**, 16333 (2019).
- A. N. Mansour, D. G. Kwabi, R. A. Quinlan, Y.-C. Lu, and Y. Shao-Horn, *J. Electrochem. Soc.*, **163**, A2911 (2016).